PIBB 生物化学与生物物理进展
Progress in Biochemistry and Biophysics
2025,52(11):2900~2915
www.pibb.ac.cn

Prediction of RNA m6A Methylation Sites in Multiple Tissues Based on Dual-branch Residual Network*

GUO Xiao-Tian[1)], GAO Wei[1)], CHEN Dan[2)], LI Hui-Min[1)**], TAN Xue-Wen[1)**]
([1)]*School of Mathematics and Computer Science, Yunnan Minzu University, Kunming* 650504, China;
[2)]*Yunnan Key Laboratory of Statistical Modeling and Data Analysis, Yunnan University, Kunming* 650500, China)

Graphical abstract

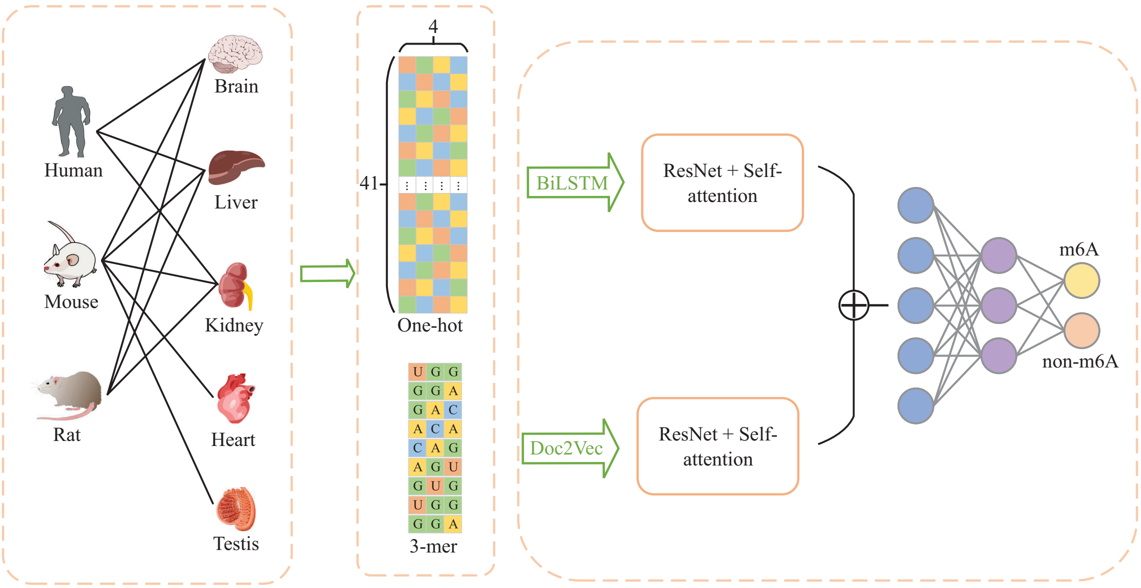

Benchmark datasets　Feature encodings　Architecture of m6A-PSRA model

Abstract **Objective** N6-methyladenosine (m6A), the most prevalent epigenetic modification in eukaryotic RNA, plays a pivotal role in regulating cellular differentiation and developmental processes, with its dysregulation implicated in diverse pathological conditions. Accurate prediction of m6A sites is critical for elucidating their regulatory mechanisms and informing drug development. However, traditional experimental methods are time-consuming and costly. Although various computational approaches have been proposed, challenges remain in feature learning, predictive accuracy, and generalization. Here, we present

---

* This work was supported by grants from The National Natural Science Foundation of China (12361104), Yunnan Fundamental Research Projects (202301AT070016, 202401AT070036), the Youth Talent Program of Xingdian Talent Support Plan (XDYC-QNRC-2022-0514), the Yunnan Province International Joint Laboratory for Intelligent Integration and Application of Ethnic Multilingualism (202403AP140014), and the Open Research Fund of Yunnan Key Laboratory of Statistical Modeling and Data Analysis, Yunnan University (SMDAYB2023004).

** Corresponding author.
LI Hui-Min. Tel: 86-871-65913115, E-mail: lihuimin_1980@126.com;
TAN Xue-Wen. Tel: 86-871-65913110, E-mail: tanxw520@163.com

Received: April 17, 2025　Accepted: August 11, 2025

m6A-PSRA, a dual-branch residual-network-based predictor that fully exploits RNA sequence information to enhance prediction performance and model generalization. **Methods** m6A-PSRA adopts a parallel dual-branch network architecture to comprehensively extract RNA sequence features *via* two independent pathways. The first branch applies one-hot encoding to transform the RNA sequence into a numerical matrix while strictly preserving positional information and sequence continuity. This ensures that the biological context conveyed by nucleotide order is retained. A bidirectional long short-term memory network (BiLSTM) then processes the encoded matrix, capturing both forward and backward dependencies between bases to resolve contextual correlations. The second branch employs a k-mer tokenization strategy (k=3), decomposing the sequence into overlapping 3-mer subsequences to capture local sequence patterns. A pre-trained Doc2vec model maps these subsequences into fixed-dimensional vectors, reducing feature dimensionality while extracting latent global semantic information *via* context learning. Both branches integrate residual networks (ResNet) and a self-attention mechanism: ResNet mitigates vanishing gradients through skip connections, preserving feature integrity, while self-attention adaptively assigns weights to focus on sequence regions most relevant to methylation prediction. This synergy enhances both feature learning and generalization capability. **Results** Across 11 tissues from humans, mice, and rats, m6A-PSRA consistently outperformed existing methods in accuracy (*ACC*) and area under the curve (*AUC*), achieving >90% *ACC* and >95% *AUC* in every tissue tested, indicating strong cross-species and cross-tissue adaptability. Validation on independent datasets—including three human cell lines (MOLM1, HEK293, A549) and a long-sequence dataset (m6A_IND, 1 001 nt)—confirmed stable performance across varied biological contexts and sequence lengths. Ablation studies demonstrated that the dual-branch architecture, residual network, and self-attention mechanism each contribute critically to performance, with their combination reducing interference between pathways. Motif analysis revealed an enrichment of m6A sites in guanine (G) and cytosine (C), consistent with known regulatory patterns, supporting the model's biological plausibility. **Conclusion** m6A-PSRA effectively captures RNA sequence features, achieving high prediction accuracy and robust generalization across tissues and species, providing an efficient computational tool for m6A methylation site prediction.

Key words N6-methyladenosine site, Doc2vec, BiLSTM, dual-branch residual network, self-attention

DOI：10.3724/j.pibb.2025.0167 **CSTR**：32369.14.pibb.20250167

RNA modification is an essential aspect in biological research, playing indispensable roles in numerous biological processes and cellular functions. To date, more than 170 different chemical modifications have been discovered in RNA[1]. These modifications significantly impact RNA function and stability. In eukaryotic RNA, N6-methyladenosine (m6A) ranks among the most abundant chemical modifications and accounts for 80% of methylation events in messenger RNA (mRNA)[2]. m6A refers to the methylation of the nitrogen atom at the N6 position of adenosine in RNA, catalyzed by methyltransferases. It is a dynamic and reversible process that maintains the homeostatic balance of m6A levels within cells through the coordinated interactions among "writers", "readers" and "erasers"[3] and has profound implications for the regulation of gene expression, cell differentiation and development.

An increasing number of studies demonstrate that regulators of m6A methylation participate in and influence the pathogenesis of various diseases. For example, overexpression of METTL3 promotes liver cancer cell proliferation and tumor growth by catalyzing m6A modification of *c-Myc* mRNA, which enhances its stability[4]. Conversely, low expression of METTL14 reduces m6A modification of *CDKN2B* (*p15INK4b*) mRNA, leading to decreased mRNA stability, disrupted cell cycle regulation, and increased gastric cancer cell proliferation[5]. High expression of ALKBH5 maintains the self-renewal capacity of glioblastoma stem cells (GSCs) and promotes malignant tumor progression by demethylating *SOX2* mRNA, thereby enhancing its stability[6]. Furthermore, elevated METTL3 expression fosters acute myeloid leukemia (AML) cell proliferation and blocks differentiation by methylating oncogenic mRNAs such as HOXA9 and MEIS1, stabilizing these transcripts and contributing to leukemia development[7]. Under heat shock conditions, METTL3 is recruited to heat shock protein (HSP) mRNA sites to add m6A modifications. YTHDF1 recognizes these modifications to enhance *HSP* mRNA translation efficiency, rapidly increasing HSP protein levels and aiding the cellular response to stress-induced damage[8]. Therefore, the rapid and accurate identification and prediction of m6A methylation sites are critical for disease treatment and contribute significantly to drug development.

Traditional biochemical experiments, such as two-dimensional thin-layer chromatography[9] and high-performance liquid chromatography[10], were initially the primary approaches used to identify m6A methylation sites. However, advancements in high-throughput sequencing technologies have gradually revealed the structural and functional roles of m6A, driving the emergence of innovative m6A detection methods such as m6A-seq[11], MeRIP-Seq[12], and PA-m6A-seq[13]. Although these methods can accurately identify m6A methylation sites, they still have several limitations. For example, the increasing volume of sequencing datasets has significantly amplified the complexity of sequence data analysis. In addition, challenges such as high costs, time-consuming procedures, and technical complexity make experimental or direct sequencing-based identification of these sites particularly difficult.

Fortunately, with the advent of the artificial intelligence era, computational models have been designed to facilitate in silico prediction for m6A sites. The fundamental principle of these methods is to utilize RNA sequences as the input for the model and predict the probability of a nucleotide “A” being an m6A site. The primary distinction among these approaches lies in the feature extraction methods applied to RNA sequences and the use of machine learning algorithms. For example, Chen *et al.* [14] developed iRNA-Methyl which utilizes the pseudo dinucleotide composition (PseDNC) feature and a support vector machine (SVM) algorithm to predict m6A methylation sites. DNN-m6A[15] builds a deep neural network (DNN) model by integrating nucleotide chemical properties, *k*-mer frequencies, position-specific scoring features, and various descriptive features of RNA sequences from multiple perspectives. The ensemble model in M6APred-EL[16] consists of three SVM classifiers that integrate features such as positional *k*-mer nucleotide propensity, physicochemical properties, and loop-structure-related hydrogen bonding characteristics for m6A site prediction. ERT-m6Apred[17] utilizes a two-stage feature selection process to evaluate seven encoding schemes, ultimately constructing a prediction model based on extreme randomized trees (ERT). M6A-BiNP[18] introduces two novel feature encoding approaches, PSP-PMI and PSP-PJMI, integrated with SVM classifiers to enhance m6A site prediction.

In addition to machine learning, deep learning models, due to their superior nonlinear fitting and pattern recognition capabilities without manual feature extraction, have outperformed traditional machine learning methods in numerous tasks. Among them, some studies employ single-model prediction methods such as Deepm6A-MT[19], TS-m6A-DL[20], and im6A-TS-CNN[21], whereas the majority adopt ensemble deep learning strategies to identify m6A methylation sites. Compared with single-model frameworks, ensemble models that combine architectures such as CNN, RNN, LSTM and GRU further improve prediction accuracy and stability, as exemplified by im6APred[22], EDLm6APred[23], EMDLP[24], DeepM6ASeq[25] and the method proposed by Li *et al.*[26].

Moreover, researchers have integrated natural language processing (NLP) techniques with deep learning to predict m6A sites. Given the similarity between natural language texts and RNA sequences as symbolic sequences, NLP’s strength in sequential data processing and feature extraction is leveraged. By treating RNA sequences as text and employing NLP techniques such as word embedding and one-hot encoding, researchers can extract position-specific information and semantic features of sequences for m6A site prediction. For example, Gene2vec[27] employs gene subsequence embedding and deep neural networks to predict mammalian m6A sites. M6A-BERT-Stacking[28] extracts RNA sequence features *via* dinucleotide indexing (DiNUCindex_RNA) and *k*-mer tokenization. This method combines residual networks (ResNet) with attention modules, BiLSTM integrated with attention mechanisms, and a pre-trained DNA-BERT model to identify m6A sites across different tissues.

Although the above-mentioned m6A site prediction methods have achieved great success, they still face several challenges: (1) when using deep learning for site prediction, some simple sequence feature encoding methods are often employed, which cannot effectively represent the original sequence information; (2) the prediction performance of existing methods, especially when applied to multiple species or tissues, requires further improvement in terms of the accuracy and generalization ability. To address this, we introduce a novel deep learning method based on a dual-branch residual network, named m6A-PSRA, to predict m6A sites across multiple mammalian species and tissues. m6A-PSRA utilizes a dual-branch residual network architecture. One branch leverages one-hot encoding and employs BiLSTM for sequence representation and feature learning, while the other branch adopts *k*-mer tokenization and utilizes the pre-trained Doc2vec model for feature extraction. Both branches incorporate ResNet architectures coupled with self-attention modules to boost feature representation accuracy and strengthen the model's generalization ability. As a result, we demonstrate that the prediction performance of m6A-PSRA is significantly improved in terms of both accuracy and robustness.

1 Materials and methods

1.1 Materials

A reliable and comprehensive benchmark dataset is essential for building an accurate and stable m6A methylation site prediction model. Aligned with previous methodologies, this study employed the benchmark datasets created by Dao *et al.*[29] to train and evaluate the proposed m6A-PSRA model. The datasets include m6A methylation sites from 11 tissues across three species: human, mouse and rat. For human, the included tissues are the brain, liver, and kidney; for mouse, they are the brain, liver, heart, testis, and kidney; and for rat, the brain, liver, and kidney are involved. Each dataset was divided into two subsets: a training set and an independent test set. All samples consisted of 41-nucleotide (nt) RNA sequences, with adenine “A” always located at the center. Sequences containing m6A sites were designated as positive samples, whereas the others served as negative controls. Each dataset contained an equal quantity of positive and negative samples. Table 1 provides detailed statistical information about the dataset.

Table 1 Statistics of benchmark datasets

Species	Tissues	Abbreviations	Training datasets		Independent test datasets	
			Positive	Negative	Positive	Negative
Human	Brain	H_B	4 605	4 605	4 604	4 604
	Kidney	H_K	4 574	4 574	4 573	4 573
	Liver	H_L	2 634	2 634	2 634	2 634
Mouse	Brain	M_B	8 025	8 025	8 025	8 025
	Heart	M_H	2 201	2 201	2 200	2 200
	Kidney	M_K	3 953	3 953	3 952	3 952
	Liver	M_L	4 133	4 133	4 133	4 133
	Testis	M_T	4 707	4 707	4 706	4 706
Rat	Brain	R_B	2 352	2 352	2 351	2 351
	Kidney	R_K	3 433	3 433	3 432	3 432
	Liver	R_L	1 762	1 762	1 762	1 762

1.2 Feature encodings

In RNA methylation site prediction, feature encoding strategies play a crucial role in the representational capacity of sequence information. The feature vectors generated by different encoding methods greatly influence the learning efficacy of machine learning models, directly impacting their generalization performance and predictive reliability. In this study, we employed two feature extraction approaches: one-hot encoding and *k*-mer tokenization.

1.2.1 One-hot encoding

The four RNA bases were processed using a one-hot encoding: A=[1,0,0,0], C=[0,1,0,0], G=[0,0,1,0], and U=[0,0,0,1]. Therefore, a sample RNA sequence with length L is converted into an $L\times4$ numeric matrix, with each row containing a single 1 and the remaining values as 0. This encoding preserves the sequential order of the bases while converting symbolic sequences into numeric forms directly processable by computational models. All RNA sequences in the dataset were encoded into matrices *via* one-hot encoding.

1.2.2 *k*-mer tokenization

To further explore latent information in RNA sequences, m6A-PSRA employed Sequence-to-Vector technology to project high-dimensional data into a low-dimensional vector space, which enhanced representation accuracy by capturing internal semantic relationships within sequences. A critical step in this process was *k*-mer tokenization, where subsequences of length *k* (termed *k*-mers) were sequentially extracted from RNA sequences. For this study, we set *k*=3. Taking the RNA sequence "AGUCUA" as an example, the resulting 3-mer segments were "AGU", "GUC", "UCU", and "CUA".

1.3 Architecture of m6A-PSRA model

In m6A-PSRA, we mainly used two residual networks to process the one-hot encoding features and the *k*-mer tokenization embedding features, respectively. The overall model architecture is illustrated in Figure 1. As shown in Figure 1a, the model consists of a dual-network architecture with two sub-networks or branches. The first sub-network (denoted as path1) contains a BiLSTM, a ResNet and a self-attention mechanism. For the one-hot encoding sequences are first fed into BiLSTM network. By processing sequences in both forward and reverse directions, the BiLSTM captures bidirectional dependencies and comprehensively learns patterns and structural features. These feature representations are further refined through a residual network using skip connections, which mitigate vanishing gradient issues in deep architectures. Finally, a self-attention layer assigns greater weight to the critical regions within the input sequence, thereby generating more refined feature representations (Figure 1b). In contrast, the second network (path2) employs a distinct approach to process sequences. It contains a Doc2vec module, a ResNet and a self-attention mechanism. First, *k*-mer tokenization divides the RNA sequences into 3-mer subsequences, and generates their vector representations. These encoded features are then fed into ResNet and a self-attention mechanism to derive an additional set of features (Figure 1c). The processed one-hot encoding features and *k*-mer tokenization features from both sub-networks are concatenated, followed by two fully connected layers that ultimately produce a two-class probability output.

The details of BiLSTM, Doc2vec, ResNet and self-attention mechanism are as follows.

1.3.1 BiLSTM

BiLSTM was proposed by Graves *et al.*[30] to address the limitations of unidirectional LSTM, which only utilizes information from the current and preceding steps, thereby missing full contextual dependencies. BiLSTM employs two LSTM networks: one processes the sequence forward, and the other backward. By integrating bidirectional information, it can more effectively capture contextual relationships.

1.3.2 Doc2vec

Doc2vec aims to map *k*-mer fragments in RNA sequences to vector representations by employing either Distributed Memory model of Paragraph Vectors (PV-DM) or Distributed Bag of Words version of Paragraph Vector (PV-DBOW)[31]. During the pre-training of m6A-PSRA, we adopted the PV-DM model. This model averages the vectors of the sequence and *k*-mer fragments to predict the next *k*-mer fragment, enabling the extraction of both local properties and global RNA sequence features. The probability distribution predicted by the PV-DM model is calculated as follows:

$$y_i = \mathrm{softmax}\left(\sum_{i=0}^{c} V_i W_{t-i} + VD + b\right) \tag{1}$$

where y_i is the input vector of the next *k*-mer fragment predicted by the model, V_i denotes the vector of the *i*-th *k*-mer fragment being processed, W_{t-i} represents the weight of the *i*-th contextual *k*-mer fragment, V is the weight of the entire sequence, D indicates the feature vector of the processed sequence, and b is the bias term.

1.3.3 ResNet

Residual networks, an enhanced form of CNNs, play a key role in deep learning, effectively addressing issues such as vanishing gradients, exploding gradients, and performance degradation in conventional CNNs[32]. As illustrated in Figure 1b, c, the residual block of m6A-PSRA operates as follows: Inputs are preprocessed *via* a standard CNN convolutional operation to capture local features, followed by max-pooling to further filter information and reduce dimensionality, thereby yielding refined feature representations. Related procedures are

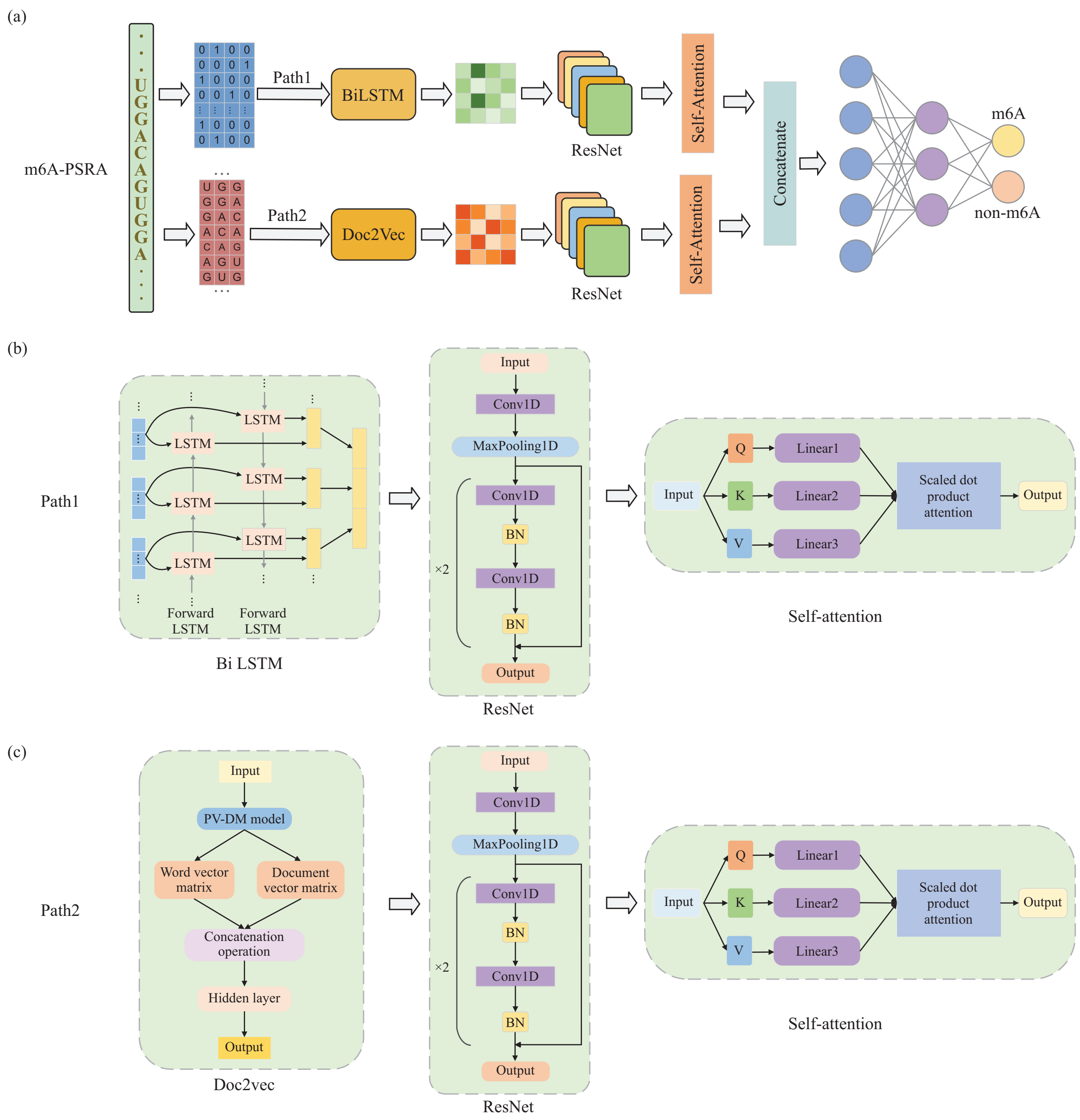

Fig. 1 Architecture of m6A-PSRA

(a) The overall framework of m6A-PSRA. Input sequences undergo parallel processing *via* path1 (a BiLSTM followed by a ResNet) and path2 (a Doc2vec followed by a ResNet). Both paths separately pass through self-attention mechanisms, and the concatenated outputs are fed into a fully connected network to classify m6A and non-m6A sites. (b) Illustration of Path1. First, a BiLSTM network is employed to capture sequence context. Second, a ResNet is used to extract deep features; it consists of one-dimensional convolutional layers (Conv1D), one-dimensional max-pooling layers (MaxPooling1D), and batch normalization layers (BN). This combination is repeated twice. Finally, a self-attention module, implemented through linear transformations and scaled dot product attention, is applied to highlight critical features. (c) Illustration of Path2. First, a Doc2Vec model is used to generate embedding features from the input sequences. Then, similar to Path1, a ResNet and a self-attention module are applied to enhance the feature representations.

implemented as follows:

$$Conv(x) = \sum_{p=1}^{P}\sum_{q=1}^{Q} w_{pq}^{k} x_{ip,q} \tag{2}$$

$$pool(x)_i = \max(x_1, x_2, x_3, \cdots, x_n)_i \tag{3}$$

1.3.4 Self-attention mechanism

Self-attention helps model to focus on critical input sequence features. In m6A-PSRA, it prioritizes essential embedded features for better representations[33]. It first receives a sequence of embedded vectors as input and generating query, key and value vectors for each. Then it computes dot products of query and all key vectors for attention scores, and normalizes scores to attention weights *via* a softmax function. Finally, it performs a weighted summation of the value vectors to generate an output that incorporates contextual information from the entire sequence. The mathematical formulas are as follows:

$$Q_i = W_1 \cdot X_i, Q_i = W_2 \cdot X_i \tag{4}$$

$$s_i = V^T \cdot \tanh(Q_i + K_i) \tag{5}$$

$$\alpha_i = \frac{\exp(s_i)}{\sum_{j=1}^{n} \exp(s_j)}, C = \sum_{i=1}^{n} \alpha_i \cdot X_i \tag{6}$$

$$Attention(Q, K, V) = \mathrm{softmax}\left(\frac{QK^T}{\sqrt{d_k}}\right)V \tag{7}$$

where W_1 and W_2 denote two weight matrices. X_i represents the feature vector at the *i*-th timestep. Q_i and K_i are the query and key, respectively. The attention score S_i is obtained by weighting the query and key matrices through a nonlinear activation function tanh, followed by multiplication with the transposed scoring weight matrix V^T. The attention weight α_i is derived by applying the softmax function to these scores. *C* denotes the final context vector.

1.4 Loss caculation

The binary cross-entropy function is utilized to calculate the loss, as presented in Equation (8):

$$Loss = \frac{1}{N}\sum_{i} -[y_i \ln p_i + (1 - y_i)\ln(1 - p_i)] \tag{8}$$

where y_i denotes the label assigned to the *i*-th instance, with 1 indicating the positive class and 0 corresponding to the negative class; p_i indicates the probability that the *i*-th instance is predicted as the positive class.

1.5 Evaluation metrics

Five commonly used evaluation metrics for classifier are employed to evaluate the model's prediction performance. They are accuracy (*ACC*), sensitivity (*SN*), specificity (*SP*), Matthews correlation coefficient (*MCC*) and area under curve (*AUC*) value. The specific calculation for these metrics are as formulas (9)−(12):

$$SN = \frac{TP}{TP + FN} \tag{9}$$

$$SP = \frac{TN}{TN + FP} \tag{10}$$

$$ACC = \frac{TP + TN}{TP + FP + TN + FN} \tag{11}$$

$$MCC = \frac{(\mathrm{TP} \times TN) - (FP \times FN)}{\sqrt{(TP + FN) \times (TP + FP) \times (TN + FN) \times (TN + FP)}} \tag{12}$$

where *TP* (true positive), *FP* (false positive), *TN* (true negative) and *FN* (false negative) refer to the counts of correctly predicted m6A sites, incorrectly predicted non-m6A sites, correctly identified non-m6A sites, and incorrectly identified m6A sites, respectively. The *AUC* value represents the area under the receiver operating characteristic (ROC) curve, varying within the range of 0 to 1. A higher *AUC* value implies more superior performance of the model.

2 Results and discussion

2.1 Detailed experimental procedure and parameter settings

The following outlines the detailed procedures and parameter settings used during the model execution.

(1) The model adopts a parallel dual-branch architecture that transforms nucleotide sequence data into two independent feature embeddings, each with a dimension of (128, 1), which are fed into the model separately.

(2) A convolutional layer with 128 filters is applied for feature learning, followed by max pooling for downsampling, which reduces the feature dimension to (64, 1).

(3) Two residual blocks are used to enhance feature representation. Each block processes input features through two parallel paths: the main path applies two consecutive convolutional layers, each followed by batch normalization to improve training efficiency; the skip path adjusts the input dimensionality to 64 using flattening and a fully connected layer. Outputs from both paths are fused *via* element-wise addition and passed through a ReLU activation function to introduce nonlinearity. The final output shape remains (64, 1).

(4) A self-attention mechanism is then introduced, in which learnable parameter matrices (W_1, W_2, V) compute cross-temporal attention weights. These weights are normalized *via* softmax to

produce importance distributions across time steps, allowing for weighted aggregation of the original features into a global contextual vector.

(5) A convolutional layer with 64 filters, followed by max pooling, further compresses the feature dimensions. After flattening, the output shape becomes (batch_size, 32). The flattened feature vectors from both branches are concatenated into a 64-dimensional vector, which is passed through a final fully connected layer with sigmoid activation to produce binary classification probabilities.

2.2 Effect of different feature encoding ways

To evidence our choice of one-hot encoding and *k*-mer encoding ways, we evaluated five classical feature encoding ways: one-hot encoding, *k*-mer encoding, Electron-Ion Interaction Pseudopotential (EIIP), Pseudo dinucleotide composition (PseDNC), and Physical and Chemical Property (PCP). We selected the optimal combination of two encoding methods based on their performance in this study. Experiments were conducted using human brain tissue data, with the results summarized in Table 2.

Table 2 clearly shows that different feature encoding combinations yield significant variations in m6A methylation site prediction performance. Among these, the combination of one-hot and *k*-mer encoding (One-hot + *k*-mer) achieved the best results, with an *ACC* of 9.70% and an *AUC* of 95.90%. This combination effectively captures sequence base distribution and conserved motif features. In contrast, the *ACC* and *AUC* values for other encoding combinations were notably lower. Based on these findings, we selected one-hot and *k*-mer encoding as the sequence encoding strategies for the two pathways in our model.

Table 2 Performance comparison of different feature encoding combinations

Feature encoding	*ACC*/%	*AUC*/%
One-hot+EIIP	89.99	94.10
One-hot+PCP	89.76	94.34
One-hot+PseDNC	81.33	90.88
One-hot+*k*-mer	9.70	95.90
EIIP+*k*-mer	79.33	85.58
PCP+*k*-mer	61.74	6.58
PseDNC+*k*-mer	91.81	95.37

2.3 Performance evaluation of m6A-PSRA

Under 10-fold cross-validation, the m6A-PSRA model exhibited superior predictive performance across different species and tissues (Table 3). All samples achieved *ACC* values exceeding 91% and *AUC* values above 95%, demonstrating robust stability and discriminative power. When classified by species, the model performed exceptionally well in humans, with an average prediction accuracy of 94.46%. Specifically, in human brain tissue, the *ACC* value was 9.82%, and the *AUC* was 95.84%. In kidney tissue, the *ACC* reached 95.26% with an *AUC* of 97.10%, while in liver tissue, the *ACC* was 95.29% and the *AUC* was 97.16%. The mouse followed closely, with an average prediction accuracy of 9.03%. Across various mouse tissues, including the brain, heart, and kidneys, both *ACC* and *AUC* remained at high levels—for example, in brain tissue, the *ACC* was 9.52% and the *AUC* was 96.15%. In contrast, the performance on rats was slightly lower, with an average prediction accuracy of 9.03%, though the metrics across different tissues remained strong. For instance, in rat brain tissue, the ACC was 9.29% and the *AUC* was 95.90%. In the tissue-specific analysis, human liver tissue achieved the best performance with an *ACC* value of 95.29%, while rat kidney had the lowest accuracy at 91.35%. Although this represented the lowest accuracy among all tissues, it still exceeded 90%, demonstrating the overall reliability of the model.

Overall, the m6A-PSRA model demonstrates high prediction accuracy across a wide range of species and tissues, along with robust generalization capabilities, effectively adapting to diverse biological environments and sample characteristics.

Table 3 Performance of m6A-PSRA under different tissues

Species	Tissues	10-fold cross-validation				
		ACC/%	*SN*/%	*SP*/%	*MCC*/%	*AUC*/%
Human	Brain	9.82	94.10	91.55	85.76	95.84
	Kidney	95.26	94.67	95.84	90.56	97.10
	Liver	95.29	96.06	94.53	90.61	97.16
Mouse	Brain	9.52	9.90	94.14	87.06	96.15
	Heart	9.83	9.48	9.19	85.86	95.53
	Kidney	91.96	95.60	88.31	84.43	96.47
	Liver	9.54	94.37	9.71	87.18	96.24
	Testis	9.31	94.99	91.63	86.73	96.07
Rat	Brain	9.29	9.21	9.37	86.71	95.90
	Kidney	91.35	95.32	87.38	8.53	96.47
	Liver	91.44	84.77	98.13	84.05	95.96

2.4 Performance of m6A-PSRA on independent datasets

To further validate the performance of m6A-PSRA, we also tested it on datasets from different human cell lines[34], specifically m6A modification datasets from the human acute myeloid leukemia cell line (MOLM13), human embryonic kidney cell line (HEK293), and human lung cancer cell line (A549). Additionally, we included the long-sequence human dataset m6A_IND[24], which features sequences of 1 001 nt. This allowed us to assess the method's effectiveness in processing long-sequence data and to further expand the validation dimensions. We systematically compared m6A-PSRA with EMDLP and CLSM6A—the methods proposed in relevant literature—across the aforementioned human cell line datasets and the m6A_IND dataset, evaluating their performance using two metrics: accuracy and *AUC*. As shown in Figure 2, on the MOLM1, HEK29, A549 cell line datasets and the m6A_IND long-sequence dataset, m6A-PSRA consistently outperformed CLSM6A and EMDLP in both accuracy and *AUC*. This superior performance is attributed to the deepened features derived from ResNet and the Soft-Attention mechanism focusing on key sequence aspects, which enable stable discrimination between m6A-modified and unmodified sites and enhance the model's robust generalization ability. By leveraging dual-path extraction of local and global sequence features and optimized model architecture, m6A-PSRA demonstrates robustness not only for short sequences but also across diverse cell lines and long-sequence scenarios.

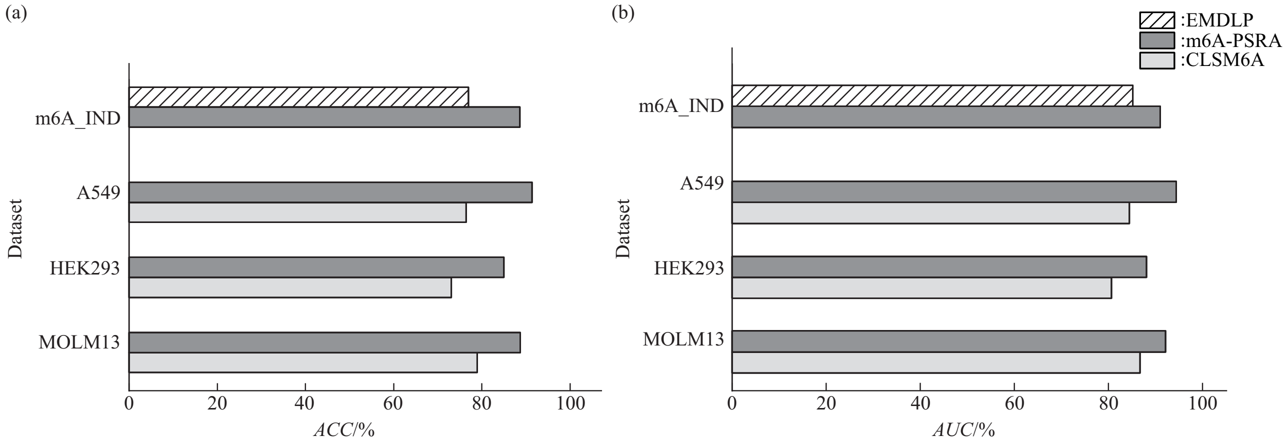

Fig. 2 Performance of m6A-PSRA on human MOLM1, HEK29, A549 cell line datasets and the m6A_IND long-sequence dataset

(a) The results of accuracy. (b) The results of *AUC*. EMDLP and CLSM6A are methods proposed respectively for predicting m6A methylation sites in human MOLM1, HEK29, A549 cell line datasets and the m6A_IND long-sequence dataset.

2.5 Comparison of m6A-PSRA with other existing methods

In evaluating m6A-PSRA's capability in m6A site prediction, we benchmarked it against five established techniques: M6A-BiNP[18], im6APred[22], Deepm6A-MT[19], Li *et al.*'s method[26] and M6A-BERT-Stacking[28]. These methods are representative advanced approaches proposed in recent years for m6A site prediction. They have all been tested on the same datasets used in this study and exhibit distinct encoding strategies and deep learning model architectures. Detailed contents are shown below in Table 4. Due to their strong representativeness and comparability, they were selected as the benchmarks for performance comparison in this research. Experiments were performed on test sets from 11 tissues across three species, with the outcomes depicted in Figure 3. The figure demonstrates that, among current methods, the m6A-BiNP approach and the method by Li *et al.* exhibit superior performance. Thus, we only present the comparison results with m6A-BiNP and Li *et al.*'s method.

Figure 3a presents the performance of different methods across various evaluation metrics in human

Table 4 A summary of the main characteristics of the compared methods for m6A site prediction

Methods	Feature encoding schemes	Classifiers
M6A-BiNP[18]	PSP-PMI, PSP-PJMI	Bi-CNN, Attention
im6APred[22]	NCP, Mono-Nucleotide Binary Encoding	CNN
Deepm6A-MT[19]	One-hot, NCP	Bi-GRU
Li *et al.*'s method[26]	One-hot	Bi-GRU
M6A-BERT-Stacking[28]	DiNUCindex_RNA, *k*-mer Word Segmentation	Resnet-CBAM, BiLSTM-Attention, DNABERT
m6A-PSRA (our method)	One-hot, *k*-mer	BiLSTM, Doc2vec, Resnet, Self-Attention

PSP-PMI: position-specific propensities and pointwise mutual information. PSP-PJMI: position-specific propensities and pointwise joint mutual information. SVM: support vector machine. NCP: nucleotide chemical property. CNN: convolutional neural networks. Bi-GRU: bidirectional recurrent neural network. DiNUCindex_RNA: Di ribonucleotide index of RNA. Resnet-CBAM: residual networks with convolutional block attention module. BiLSTM-Attention: bidirectional long short-term memory with attention. DNABERT: pre-trained bidirectional encoder representations from transformer model for DNA-language.

brain, kidney, and liver tissues. Compared with m6A-BiNP and Li *et al.*'s methods, m6A-PSRA generally demonstrates superior performance across all metrics in all three tissues. For example, in terms of *ACC*, m6A-PSRA consistently exceeded 90%, reaching up to approximately 94% across all three tissues. Regarding the *SN* metric, m6A-PSRA demonstrated strong ability to identify positive samples, significantly outperforming m6A-BiNP (particularly in human brain tissue). For *SP*, m6A-PSRA maintained stable performance and was only slightly inferior to m6A-BiNP in human brain tissue, with the minimal gap indicating that it remained competitive. The *MCC* scores further highlighted its robust overall performance, and the *AUC* values also surpassed those of the other methods. In the human independent test set, m6A-PSRA exhibits excellent performance across all metrics in the 11 tissues, highlighting its strong generalizability.

In the mouse independent test set (Figure 3b), m6A-PSRA demonstrated superior predictive performance. With the exception of slightly lower *SP* in the M_H and M_L tissues, and a slightly lower *AUC* in the M_H tissue compared to m6A-BiNP, m6A-PSRA achieved the highest values in *ACC*, *SN*, *SP*, *MCC*, and *AUC* across all other tissues. Furthermore, compared to Li *et al.*'s method, m6A-PSRA showed consistently higher predictive accuracy across various tissues. For example, For example, the *ACC* values for Li *et al.* and m6A-PSRA in mouse tissues ranged from 87% to 91% and from 91% to 95%, respectively, while the *AUC* values ranged from 91% to 94% and from 95% to 97%. These results indicate that m6A-PSRA not only achieves higher accuracy but also significantly reduces the variability of evaluation metrics, demonstrating more stable performance and stronger generalization capability in predicting m6A methylation sites in mouse tissues.

Figure 3c illustrates the performance of various approaches on the independent test set for rat tissues. In the R_K tissue, m6A-PSRA achieved the highest *AUC* value. In R_B and R_L tissues, although its *AUC* values were slightly lower than those achieved by m6A-BiNP, they still exceeded 95% and significantly outperformed other methods. m6A-PSRA also attained the highest *ACC* values across all three rat tissues, demonstrating its effectiveness in predicting m6A methylation sites in rats. This further validates the method's superior generalization capability.

Overall, across the independent test sets of human, mouse, and rat tissues, the m6A-PSRA model consistently outperformed the method proposed by Li *et al.*, as well as other existing approaches, across multiple evaluation metrics. The m6A-PSRA model not only achieves higher accuracy and improved sensitivity in identifying positive samples, but also maintains stable performance with reduced variability across evaluation metrics. These findings clearly demonstrate its superior performance and robust generalization, making m6A-PSRA a promising approach for predicting m6A methylation sites.

2.6 Ablation study

To comprehensively examine the contribution of each component of m6A-PSRA, we conducted ablation studies by selectively removing them. Specifically, we focused on: (1) the impact of different branches, (2) the impact of the BiLSTM module, (3) the impact of residual networks, and (4) the impact of the self-attention mechanism. *ACC* was used to compare the effectiveness of the different

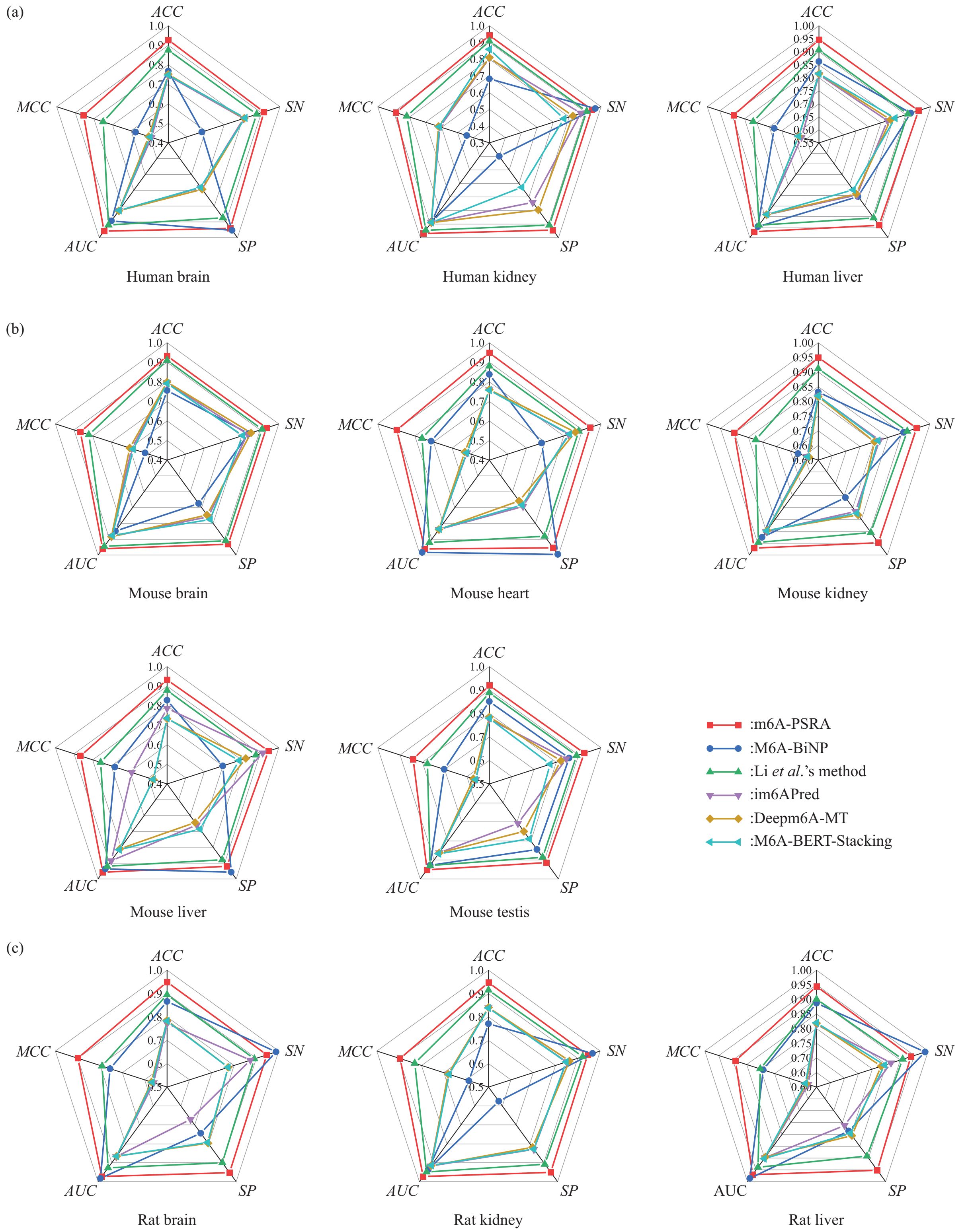

Fig. 3 Performance comparisons with existing methods across 11 tissues

(a) Performance comparision with existing methods on human tissues. (b) Performance comparison with existing methods on mouse tissues. (c) Performance comparison with existing methods on rat tissues.

model variants.

To explore the impact of different pathways, we compared m6A-PSRA with two sub-models, named Only P1 (with the path2 removed) and Only P2 (with the path1 removed). As illustrated in Figure 4a, the full m6A-PSRA model significantly outperformed both single-branch variants across most tissues, demonstrating notable improvements in *ACC*. The only exception was in the rat brain tissue (R_L), where the *ACC* of m6A-PSRA was slightly lower than that of Only P1. m6A-PSRA outperforms other methods by effectively integrating local features derived from one-hot encoding and BiLSTM, as well as global features extracted *via* Doc2vec.

To validate the importance of BiLSTM within the model, we conducted ablation experiments from two aspects: (1) removing the BiLSTM module from m6A-PSRA to create a sub-model, named "Model without BiLSTM"; and (2) replacing BiLSTM with a fully connected layer to create "Model [BiLSTM→FC]". The second approach aimed to preserve the model's overall structure while minimizing the impact of drastic parameter reduction. As shown in Figure 4b, compared to the original m6A-PSRA, over half of the tissues exhibited varying *ACC* declines after removing or replacing BiLSTM. Specifically, "Model without BiLSTM" showed ~2% drops in M_B, M_H, and R_B, while "Model [BiLSTM→FC]" had a~12% decrease in R_B. These results confirm BiLSTM's positive role in enhancing performance across most tissues, as it captures sequential temporal dependencies to improve prediction accuracy.

To evaluate the ResNet and self-attention modules, we performed additional ablation experiments. For ResNet, we either removed it to create "Model without ResNet" or replaced it with a CNN to form "Model [ResNet→CNN]". As shown in Figure 4c, removing ResNet caused significant *ACC* drops (exceeding 20% in some tissues), while replacing ResNet with CNN also led to performance declines across tissues, confirming ResNet's critical role. For self-attention, we removed the mechanism to construct "Model without SelfAtt"; Figure 4d shows

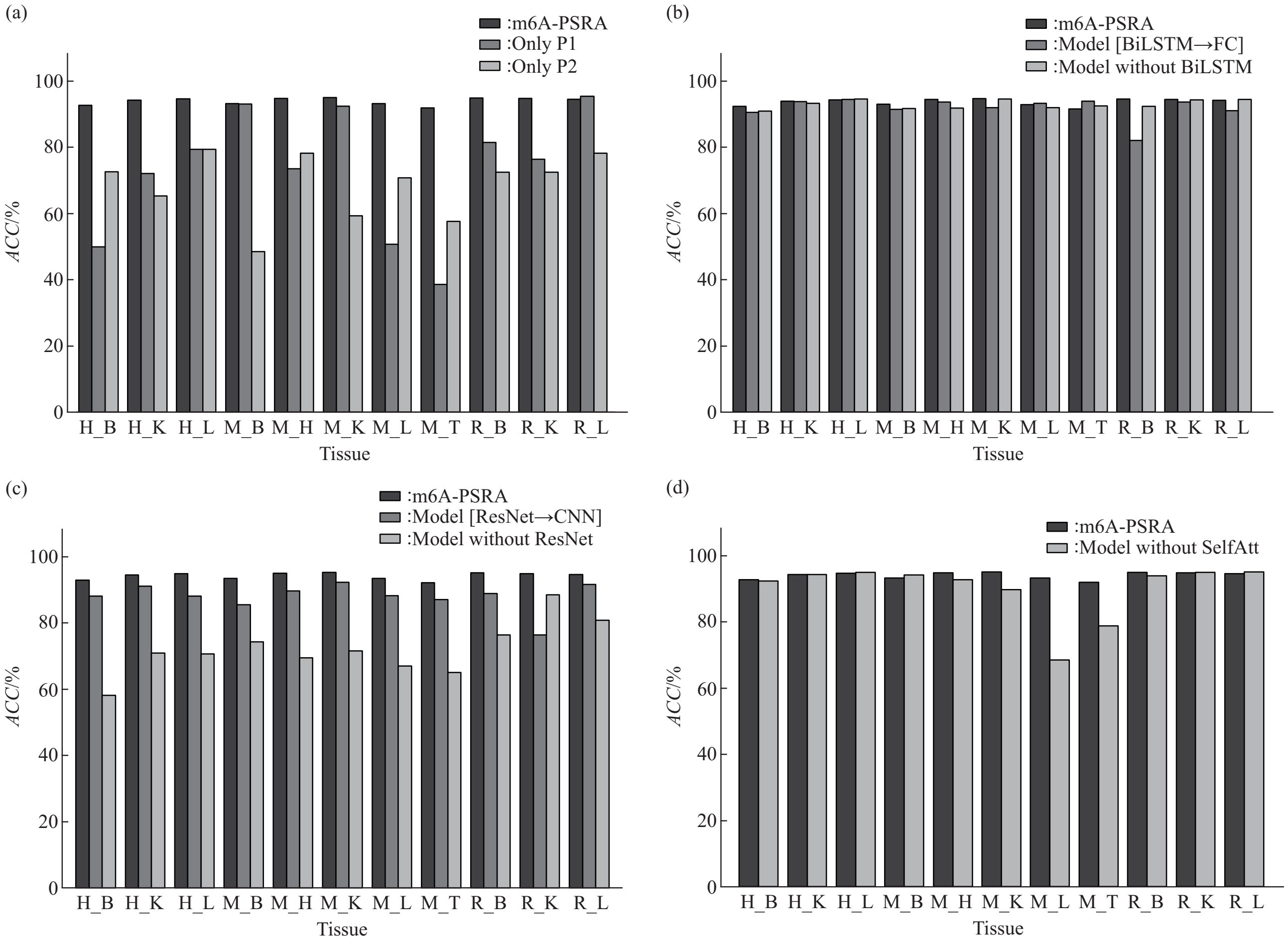

Fig. 4 Bar charts comparing ablation studies with m6A−PSRA on *ACC*

(a) Comparison of m6A-PSRA with two submodels, Only P1 and Only P. (b) Comparison of m6A-PSRA with Model [BiLSTM→FC] and Model without BiLSTM. (c) Comparison of m6A-PSRA with Model [ResNet→CNN] and Model without ResNet. (d) Comparison of m6A-PSRA with Model without SelfAtt. The specific meanings of H_B, H_K, H_L, M_B, M_H, M_K, M_L, M_T, R_B, R_K, R_L are shown in Table 1.

minimal *ACC* changes in most tissues but significant declines in specific mouse tissues (*e.g.*, M_L, M_T), suggesting its role in enhancing generalization. These results underscore the indispensable contributions of both modules to model performance.

Notably, after removing the BiLSTM module, the performance declined in over half of the tissues, but the decrease was relatively small, indicating that ResNet and Self-Attention are the core components of m6A-PSRA. Interestingly, removing ResNet or Self-Attention sometimes improved performance in certain tissues compared to retaining only a single path. This reflects the advantages of multi-path fusion — eliminating one path can reduce interference and enhance the contribution of others, leading to better overall results. This further highlights that the effectiveness of multi-path fusion relies on the complementarity and interaction of different modules, rather than on any single component's absolute importance.

2.7 Motif analysis

To illustrate the position-specific differences between m6A and non-m6A sequences in the baseline dataset, we used two-sample logo software[35]. According to Figure 5, the sequence features around potential modification sites are presented through a 41-nucleotide window with the modification site at the center. Nucleotides above the horizontal axis

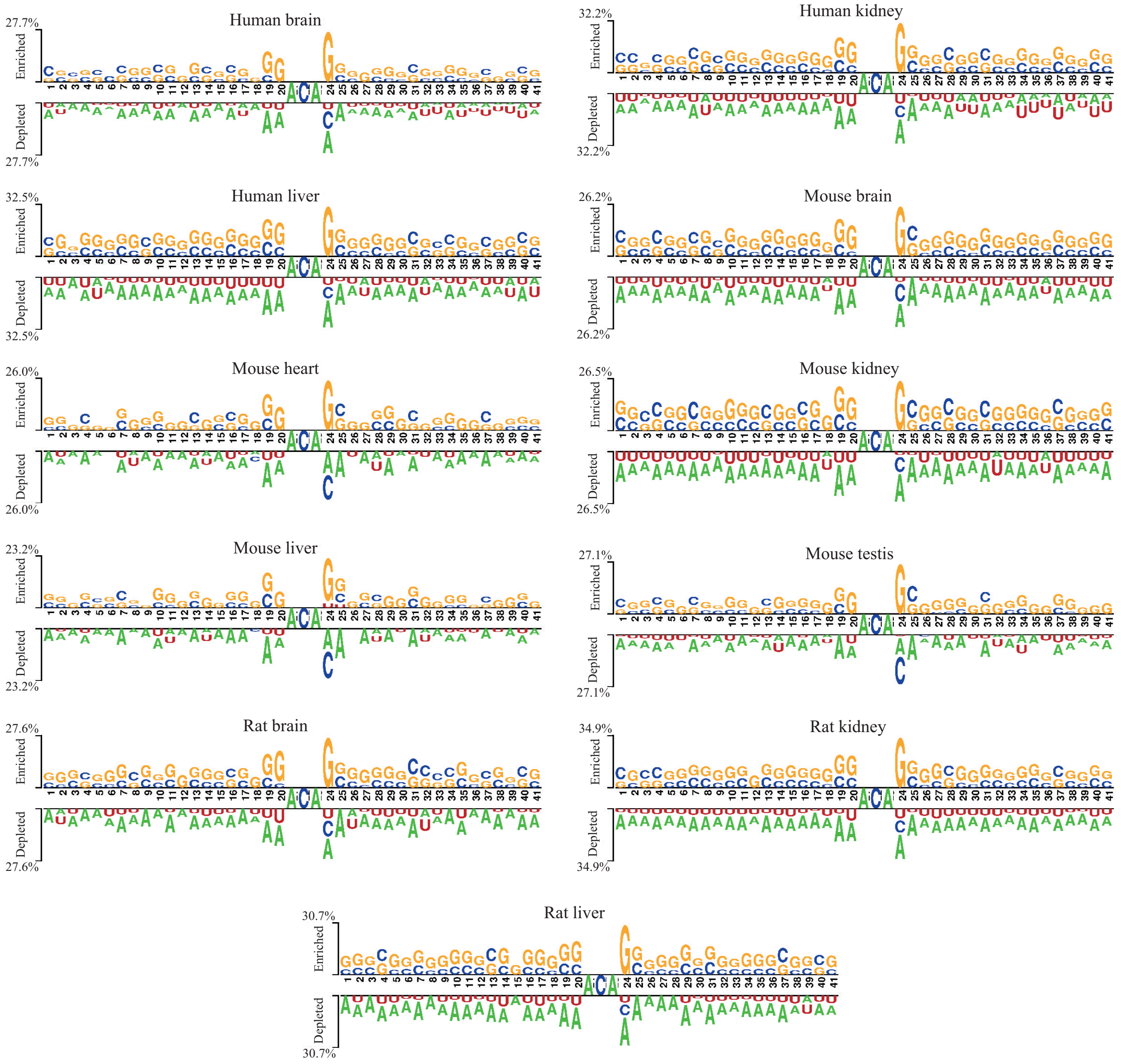

Fig. 5　Nucleotide composition preferences between positive and negative samples on the baseline datasets

represent bases significantly enriched in positive samples, while those below represent bases significantly depleted. Analysis indicates a clear difference in the sequence context between m6A modification sites and non-m6A sites: m6A sites tend to exhibit enrichment for guanine (G) and cytosine (C) in their vicinity, while non-m6A sites show a higher frequency of uracil (U) and adenine (A) aggregation. This finding supports the feasibility of developing computational models to predict potential m6A sites using sequence information.

3 Conclusion

As a pivotal epigenetic modification, m6A methylation significantly influences diverse cellular functions, necessitating precise identification of m6A loci to advance RNA methylation research. Although numerous computational methods have been developed, there is still room for improvement in feature extraction, prediction accuracy, and the model's generalization ability. Therefore, we propose m6A-PSRA, a novel deep learning framework based on a dual-branch residual network, capable of predicting m6A sites across multiple species and tissue types. One branch of m6A-PSRA utilizes one-hot encoding combined with a BiLSTM network for feature learning, while the other employs *k*-mer tokenization together with the Doc2vec model for feature extraction. Both pathways incorporate ResNet and self-attention mechanisms to improve feature learning and enhance the model’s generalization capability. These improvements will facilitate the development of a more comprehensive and reliable m6A prediction system. The source code and supporting datasets of m6A-PSRA are publicly deposited in the GitHub repository (https://github.com/gxiaot/m6A-PSRA) and are accessible to the public.

Although m6A-PSRA demonstrates strong performance in predicting m6A methylation sites, it still faces critical challenges and technical limitations. First, the current methodology primarily relies on known experimental data and sequence features. However, existing datasets exhibit significant sample imbalance—for example, there is a severe shortage of m6A data in certain low-abundance tissues or cell types, which may reduce the model’s prediction accuracy for novel or underrepresented features. Second, analytical frameworks based on single-omics data may fail to comprehensively model the complex regulatory network of m6A modification. In future work, we plan to advance in three directions. (1) Exploring the application of transfer learning algorithms to transfer knowledge acquired from species with abundant data (*e.g.*, human and mouse datasets) to data-scarce species (*e.g.*, monkey), aiming to achieve effective prediction of RNA modification sites in these species. This approach could address the challenge of limited data availability in certain species. (2) Integrating tissue/cell-specific methylation data (*e.g.*, MeRIP-seq, miCLIP-seq) into the predictive model and training algorithms to directly map sequence features to tissue-specific m6A modification sites. Subsequent experimental validation using representative tissue-derived cell lines will confirm how tissue microenvironments regulate methylation patterns. (3) Enhancing model interpretability constitutes a key direction. This involves elucidating the relationship between critical sequence regions and prediction outcomes, thereby enhancing the credibility of the results and providing valuable insights for constructing m6A regulatory networks and downstream functional analyses.

References

[1] Boccaletto P, Stefaniak F, Ray A, *et al*. MODOMICS: a database of RNA modification pathways. 2021 update. Nucleic Acids Res, 2022, **50**(D1): D231-D235

[2] Han W, Zhao Y, Zhao R. Progress in studies on biological properties of stem cells modified by mRNA m6A methylation. Chinese Journal of Tissue Engineering Research, 2023, **27**(10): 1584

[3] Frye M, Harada B T, Behm M, *et al*. RNA modifications modulate gene expression during development. Science, 2018, **361**(6409): 1346-1349

[4] Liu J, Jiang K. METTL3-mediated maturation of miR-589-5p promotes the malignant development of liver cancer. J Cell Mol Med, 2022, **26**(9): 2505-2519

[5] Shi B, Liu W W, Yang K, *et al*. The role, mechanism, and application of RNA methyltransferase METTL14 in gastrointestinal cancer. Mol Cancer, 2022, **21**(1): 163

[6] Zhang S, Zhao B S, Zhou A, *et al*. m^{6}A demethylase ALKBH5 maintains tumorigenicity of glioblastoma stem-like cells by sustaining FOXM1 expression and cell proliferation program. Cancer Cell, 2017, **31**(4): 591-606.e6

[7] Sang L, Wu X, Yan T, *et al*. The m^{6}A RNA methyltransferase METTL3/METTL14 promotes leukemogenesis through the mdm2/p53 pathway in acute myeloid leukemia. J Cancer, 2022,

13(3): 1019-1030

[8] Yu J, Li Y, Wang T, *et al*. Modification of N6-methyladenosine RNA methylation on heat shock protein expression. PLoS One, 2018, **13**(6): e0198604

[9] Jia G, Fu Y, Zhao X, *et al*. N6-methyladenosine in nuclear RNA is a major substrate of the obesity-associated FTO. Nat Chem Biol, 2011, **7**(12): 885-887

[10] Zheng G, Dahl J A, Niu Y, *et al*. ALKBH5 is a mammalian RNA demethylase that impacts RNA metabolism and mouse fertility. Mol Cell, 2013, **49**(1): 18-29

[11] Dominissini D, Moshitch-Moshkovitz S, Schwartz S, *et al*. Topology of the human and mouse m6A RNA methylomes revealed by m6A-seq. Nature, 2012, **485**(7397): 201-206

[12] Meyer K D, Saletore Y, Zumbo P, *et al*. Comprehensive analysis of mRNA methylation reveals enrichment in 3' UTRs and near stop codons. Cell, 2012, **149**(7): 1635-1646

[13] Chen K, Lu Z, Wang X, *et al*. High-resolution N (6)-methyladenosine (m(6)A) map using photo-crosslinking-assisted m(6) A sequencing. Angew Chem Int Ed, 2015, **54**(5): 1587-1590

[14] Chen W, Feng P, Ding H, *et al*. iRNA-Methyl: identifying N(6)-methyladenosine sites using pseudo nucleotide composition. Anal Biochem, 2015, **490**: 26-33

[15] Zhang L, Qin X, Liu M, *et al*. DNN-m6A: a cross-species method for identifying RNA N6-methyladenosine sites based on deep neural network with multi-information fusion. Genes, 2021, **12**(3): 354

[16] Wei L, Chen H, Su R. M6APred-EL: a sequence-based predictor for identifying N6-methyladenosine sites using ensemble learning. Mol Ther Nucleic Acids, 2018, **12**: 635-644

[17] Govindaraj R G, Subramaniyam S, Manavalan B. Extremely-randomized-tree-based prediction of N^6-methyladenosine sites in *Saccharomyces cerevisiae*. Curr Genomics, 2020, **21**(1): 26-33

[18] Wang M, Xie J, Xu S. M6A-BiNP: predicting N^6-methyladenosine sites based on bidirectional position-specific propensities of polynucleotides and pointwise joint mutual information. RNA Biol, 2021, **18**(12): 2498-2512

[19] Huang G, Huang X, Jiang J. Deepm6A-MT: a deep learning-based method for identifying RNA N6-methyladenosine sites in multiple tissues. Methods, 2024, **226**: 1-8

[20] Abbas Z, Tayara H, Zou Q, *et al*. TS-m6A-DL: tissue-specific identification of N6-methyladenosine sites using a universal deep learning model. Comput Struct Biotechnol J, 2021, **19**: 4619-4625

[21] Liu K, Cao L, Du P, *et al*. im6A-TS-CNN: identifying the N^6-methyladenine site in multiple tissues by using the convolutional neural network. Mol Ther Nucleic Acids, 2020, **21**: 1044-1049

[22] Luo Z, Lou L, Qiu W, *et al*. Predicting N6-methyladenosine sites in multiple tissues of mammals through ensemble deep learning. Int J Mol Sci, 2022, **23**(24): 15490

[23] Zhang L, Li G, Li X, *et al*. EDLm^{6}APred: ensemble deep learning approach for mRNA m^{6}A site prediction. BMC Bioinformatics, 2021, **22**(1): 288

[24] Wang H, Liu H, Huang T, *et al*. EMDLP: ensemble multiscale deep learning model for RNA methylation site prediction. BMC Bioinformatics, 2022, **23**(1): 221

[25] Zhang Y, Hamada M. DeepM6ASeq: prediction and characterization of m6A-containing sequences using deep learning. BMC Bioinformatics, 2018, **19**(Suppl 19): 524

[26] Li H M, Chen P H, Tang Y, *et al*. Prediction of m6A methylation sites in mammalian tissues based on a double-layer BiGRU network. Prog Biochem Biophys, 2023, **50**(12): 3032-3044

[27] Zou Q, Xing P, Wei L, *et al*. Gene2vec: gene subsequence embedding for prediction of mammalian N^6-methyladenosine sites from mRNA. RNA, 2019, **25**(2): 205-218

[28] Li Q, Cheng X, Song C, *et al*. M6A-BERT-stacking: a tissue-specific predictor for identifying RNA N6-methyladenosine sites based on BERT and stacking strategy. Symmetry, 2023, **15**(3): 731

[29] Dao F Y, Lv H, Yang Y H, *et al*. Computational identification of N6-methyladenosine sites in multiple tissues of mammals. Comput Struct Biotechnol J, 2020, **18**: 1084-1091

[30] Graves A, Schmidhuber J. Framewise phoneme classification with bidirectional LSTM and other neural network architectures. Neural Netw, 2005, **18**(5/6): 602-610

[31] Le Q, Mikolov T. Distributed representations of sentences and documents//Xing E P, Jebara T. Proceedings of the 31st International Conference on Machine Learning: 32. Beijing, China: PMLR, 2014: 1188-1196

[32] He K, Zhang X, Ren S, *et al*. Deep residual learning for image recognition//IEEE. 2016 IEEE Conference on Computer Vision and Pattern Recognition (CVPR). Las Vegas, NV, USA: IEEE, 2016: 770-778

[33] Vaswani A, Shazeer N, Parmar N, *et al*. Attention is all you need//Guyon I, Luxburg U V, Bengio S, *et al*. Advances in Neural Information Processing Systems: 30. Long Beach, CA, USA: Curran Associates, Inc., 2017: 5998-6008

[34] Zhang Y, Wang Z, Zhang Y, *et al*. Interpretable prediction models for widespread m6A RNA modification across cell lines and tissues. Bioinformatics, 2023, **39**(12): btad709

[35] Vacic V, Iakoucheva L M, Radivojac P. Two Sample Logo: a graphical representation of the differences between two sets of sequence alignments. Bioinformatics, 2006, **22**(12): 1536-1537

基于双分支残差网络的多组织RNA m6A 甲基化位点预测*

郭晓甜[1)] 高 伟[1)] 陈 丹[2)] 李慧敏[1)**] 谭学文[1)**]
（[1)] 云南民族大学数学与计算机科学学院，昆明 650504；
[2)] 云南大学云南省统计建模与数据分析重点实验室，昆明 650500）

摘要 目的 N6-甲基腺苷（m6A）是真核生物 RNA 上最普遍的表观遗传修饰。它在调控细胞分化和发育过程中起着关键的作用，并且与许多疾病的病理机制相关。m6A 位点的精确预测对解析其调控机制及指导药物设计至关重要。然而，传统的生物实验方法通常耗时长且成本高昂。尽管目前已开发出多种m6A位点预测的计算方法，但这些方法在特征学习、预测准确性和泛化能力方面仍有一定改进空间。本文提出一种基于双分支残差网络的m6A位点预测算法——m6A-PSRA，旨在充分利用RNA序列的特征信息，提高m6A位点预测的准确性和模型的泛化能力。**方法** m6A-PSRA使用双分支网络架构，其中一条分支通过One-hot编码对序列进行编码，并利用双向长短期记忆网络（BiLSTM）进行特征学习，另一条分支通过*k*-mer分词编码，并利用预训练模型Doc2vec进行特征学习。在特征学习过程中，两条分支网络均整合残差网络（ResNet）和自注意力机制，以增强特征学习的准确性和模型的泛化能力。**结果** 在人类、小鼠和大鼠共11个组织中，m6A-PSRA对m6A位点的预测准确率（*ACC*）和曲线下面积（*AUC*）值均优于其他方法。特别地，其在各个组织的*ACC*值和*AUC*值分别超过90%和95%。消融实验也验证了m6A-PSRA具有较高的m6A位点预测准确性和泛化能力。**结论** m6A-PSRA能有效捕获RNA序列特征，具备较高的预测精度和优异的泛化性能，可实现跨组织的高效m6A甲基化位点预测。

关键词 N6-甲基腺苷位点，Doc2vec，BiLSTM，双分支残差网络，自注意力
中图分类号 TP391，Q52 **DOI**：10.3724/j.pibb.2025.0167 **CSTR**：32369.14.pibb.20250167

---

* 国家自然科学基金（12361104），云南省基础研究计划（202301AT070016，202401AT070036），兴滇人才支持计划青年人才项目（XDYC-QNRC-2022-0514），云南省民族多语种智能融合与应用国际联合实验室（202403AP140014）和云南省统计建模与数据分析重点实验室开放课题（SMDAYB2023004）资助。

** 通讯联系人。
李慧敏 Tel：0871-65913115，E-mail：lihuimin_1980@126.com
谭学文 Tel：0871-65913110，E-mail：tanxw520@163.com

收稿日期：2025-04-17，接受日期：2025-08-11